Available online at www.sciencedirect.com
SCIENCE DIRECT®
Acta Materialia 52 (2004) 2395–2406
Acta MATERIALIA
www.actamat-journals.com

# Fracture mechanisms of the *Strombus gigas* conch shell: II-micromechanics analyses of multiple cracking and large-scale crack bridging

Shekhar Kamat [a], Hannes Kessler [b], Roberto Ballarini [c,*], Maissarath Nassirou [a], Arthur. H. Heuer [a]

[a] *Department of Materials Science and Engineering, Case Western Reserve University, 10900 Euclid Avenue, Cleveland, OH 44106, USA*
[b] *Institute of Solid State Mechanics, University of Technology Dresden, D-01062 Dresden, Germany*
[c] *Department of Civil Engineering, Case Western Reserve University, 10900 Euclid Avenue, Cleveland, OH 44106, USA*

Received 18 July 2003; received in revised form 23 January 2004; accepted 23 January 2004

**Abstract**

Micromechanics analyses of the dominant energy-dissipating mechanisms responsible for the resistance to catastrophic fracture of the aragonitic shell of the giant Queen conch, *Strombus gigas*, are presented. The crossed lamellar microstructure of the shell is associated with a work of fracture that is three orders of magnitude higher than that of non-biogenic aragonite [J. Mater. Sci. 6 (1996) 6583]. Previous energy-based models predict that multiple "tunnel" cracks in the weak layers of the shell account for a factor of 20 of this increase in fracture energy. We show that the additional factor of $\gtrsim 300$ results from the synergy between the tunnel cracking and crack bridging mechanisms, analogous to multiple energy dissipating mechanisms observed in brittle matrix composites. The theoretical models demonstrate that the microstructure of the shell of *S. gigas* is such that potential cracks evolve towards the desirable non-catastrophic ACK (Aveston–Cooper–Kelly) [Properties of fiber composites, Conference Proceedings 15, National Physical Laboratory, IPC Science and Technology Press, 1971] limit, a situation in which all bridging ligaments remain intact along the crack wakes. Load–deflection experiments at temperatures ranging from −120 to 200 °C suggest that a glass transition occurs within the organic (proteinaceous) phase at ~175 °C, and demonstrate the critical role that this organic "matrix" plays in the resistance of the shell to catastrophic crack propagation.
© 2004 Acta Materialia Inc. Published by Elsevier Ltd. All rights reserved.

*Keywords:* *Strombus gigas*; Crack bridging; Tunnel cracking; Work of fracture; Laminated composites

## 1. Introduction

The aragonitic shell of the giant pink Queen conch, *Strombus gigas*, is characterized by high toughness and moderate strength, a direct result of an exquisite microarchitecture that contains structure over five length scales (Fig. 1). The coarsest structures are the inner, middle, and outer layers, which are oriented in either "weak" or "tough" orientations with respect to the direction of potential catastrophic crack propagation. Sequential cracking of the weak and strong layers of the shell occur during crack propagation, and it is necessary to partition the energy dissipated during fracture into these two processes; this is done here through quantitative micromechanics modeling. The theoretical predictions have been corroborated by experimental fracture toughness and acoustic emission data, as well as in situ crack propagation studies that guided the theoretical developments [4–8].

Multiple "tunnel" cracking emanating from large flaws in the weaker layers was theoretically modeled in our earlier work [5,6], and characterizes the mechanical response for relatively low loads. However, this type of cracking accounts for only a relatively small fraction of the mechanical energy required to completely fracture the shell. A much larger portion of the energy dissipated

* Corresponding author. Tel.: +1-216-368-2963; fax: +1-216-368-5229.
*E-mail address:* rxb7@po.cwru.edu (R. Ballarini).

1359-6454/$30.00 © 2004 Acta Materialia Inc. Published by Elsevier Ltd. All rights reserved.
doi:10.1016/j.actamat.2004.01.030

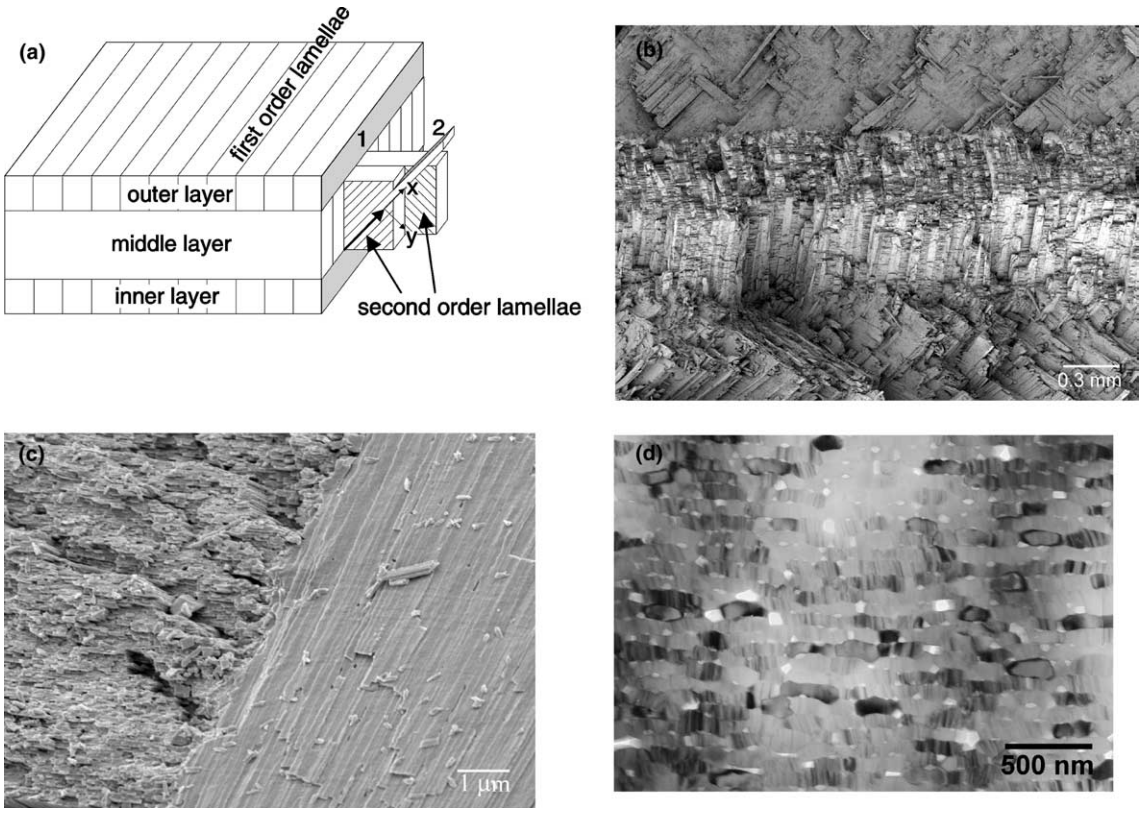


Fig. 1. (a) Schematic drawing of the microstructure of the conch shell. The bulk of the shell in mature animals contain three layers, as depicted here. Each layer contains first-order, second-order and third-order lamellae. The twinned third-order lamellae are not shown in this drawing, which emphasizes the ±90° orientation of second-order lamellae within adjacent first-order lamellae. (Second-order lamellae are only shown for two first-order lamellae in the middle layer.) The twinned third-order lamellae are the basic building blocks of the structure [3]. The first-order interfaces are weak and favor multiple microcracking in the inner and outer (weak) layers, whereas second-order interfaces favor crack deflection in the middle (tough) layer, as indicated by the bold arrow. The crack tip coordinate system shown by the less-prominent arrows $(x, y)$ appears again in Fig. 9. The layers are 0.5–2 mm thick; the first-order lamellae are 5–60 μm thick and many μm wide; the second-order lamellae 5–30 μm thick and 5–60 μm wide; and the third-order lamellae 60–130 nm thick and 100 nm wide. All third-order lamellae are surrounded by sheaths of protein; similar proteinaceous material some 10–320 nm in thickness comprise the interfaces separating second-order and first-order lamellae, as well as the layer interfaces [3]; (b) and (c) are SEM micrographs; the layer structure is easily discerned by the roughness resulting from cracks propagating parallel or perpendicular to first-order lamellar interphases in the middle layer. The rough/smooth transition in adjacent first-order lamellae is shown at high magnification in (c); finally, (d) is a TEM micrograph of a second-order lamella taken in an "end-on" orientation. Individual twinned third-order lamellae are revealed by diffraction contrast; the striped vertical features are twin boundaries. Although not apparent in this image, each third-order lamella is encased in a proteinaceous sheath; globular protein is also present [3].

during fracture of the shell is associated with crack bridging and microcracking in the "tougher" layer; this enhanced toughening arises from the ±45° orientation of the second-order lamellae in that layer (Fig. 1). This paper presents: (i) further analysis of multiple tunnel cracking that considers the possibility of growth of small flaws in the weaker layer, (ii) a micromechanics-based crack bridging model for the tougher layer, (iii) the use of this model in a non-linear bridged-crack fracture mechanics analysis that successfully predicts the essence of the experimental load–deflection curves, and (iv) the results of four point bend tests in a temperature controlled chamber at temperatures ranging from −120 to 200 °C, which illustrate the critical role played by the proteinaceous interphase. The work of fracture, defined as the total energy dissipated in the fracture process, divided by the fracture surface area, is an important parameter that will be referred to in subsequent discussion.

## 2. Multiple cracking in the "weak" layer

Enhanced energy dissipation by multiple crack formation during fracture of unnotched samples was considered in our earlier work [5,6]. Specifically, we modeled the slightly simplified plane strain configuration of a two-layer composite subjected to a prescribed applied strain $\varepsilon$ (Fig. 2). The "tough" and "weak" layers are assumed to be of equal thicknesses, $t_1 = t_2 = w/2$, and to have equal Young's modulus, $E$ and Poisson's ratio, $v$. The fracture toughness of these layers are $K_{c1}^{\text{eff}}$

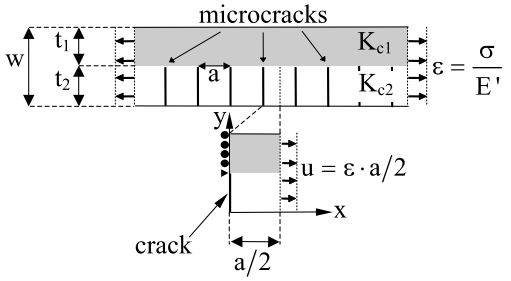


Fig. 2. Simplified two-layer composite with microcracks of average crack distance $a$. The lower portion of the figure shows the representative unit cell with a single microcrack for the finite element model. The applied strain ($\varepsilon$) is realized as a prescribed displacement, $u = \varepsilon \cdot a/2$.

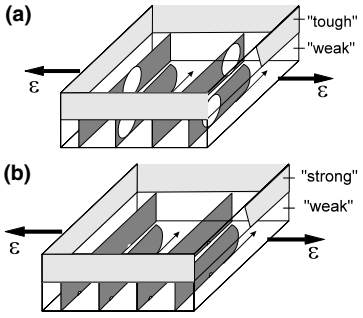


Fig. 3. Strain-energy based cracking criterion (a) in comparison to the stress-based cracking criterion (b) for tunnel crack propagation in a weak layer. The stress-based criterion describes a situation when cracks are initiated in the weak layer from small pre-existing surface flaws. The strain-energy criterion applies when cracks can grow from large pre-existing flaws. The pre-existing flaws are represented by the light regions. The direction of crack tunneling along the specimen thickness is indicated by the small arrows.

and $K_{c2}$, respectively, with $K_{c1}^{\text{eff}} > K_{c2}$. $K_{c2}$ represents the fracture toughness of the proteinaceous interfaces between first-order aragonitic lamellae, whereas the larger $K_{c1}^{\text{eff}}$ represents an effective initiation toughness associated with the extension of the tunnel cracks into the tough layer at higher loads.

As detailed in the next section, $K_{c2}$ can be related to the energy required to multiply crack the weak layer as a result of the tunneling across its width of relatively large flaws (steady-state crack propagation associated with a crack driving force that depends on $t_1/t_2$ but not on the length of the tunnel crack [9]), or to the energy required to produce the multiple cracking from relatively small surface flaws that grow to the interface between the strong and weak layers and concomitantly across the layer width (propagation whose driving force depends on the initial length of surface cracks).

It is assumed that cleavage of the proteinaceous interfaces in both layers occurs in a brittle fashion at a critical value of the crack–tip energy release rate, $J_{\text{c}}^{\text{int}} = 2\gamma_{\text{int}}$, where $\gamma_{\text{int}}$ is the surface energy. The Irwin relations between the crack–tip parameters is $J_{\text{c}}^{\text{int}} = K_{c2}^2/E' = 2\gamma_{\text{int}}$, with $E' = E/(1-\nu^2)$. However, the total energy release rate associated with crack extension in the tough layer is given by $J = J_{\text{c}}^{\text{int}} + J_{\text{b}}$, where $J_{\text{b}} = \int_0^{\Delta u_0} \sigma(\Delta u)\,\mathrm{d}(\Delta u)$. $\sigma(\Delta u)$, the crack surface traction that resists the crack opening displacement $\Delta u$, is operative up to the critical crack opening displacement $\Delta u_0$, or alternatively, up to a limiting ligament strength, $\sigma_0$. As discussed subsequently, the ratio $J_{\text{c}}^{\text{int}}/J_{\text{b}}$ greatly influences whether cracks propagate catastrophically or non-catastrophically.

When this model was formulated, the assumption of elastic homogeneity and isotropy was believed to be a simplification. However, subsequent laminate theory calculations [7] indicated that the shell is in fact nearly isotropic, with an effective modulus close to the experimentally measured value, $E' = 37$ GPa.

Fig. 3(a) is a schematic drawing that represents a physical model of multiple cracking for the two-layer composite where the applied strain, $\varepsilon$, drives a number of cracks from initial defects; these defects may be large, as in Fig. 3(a), or small, as represented in Fig. 3(b). Cracks along the interfaces between first-order lamellae in the weak layers "tunnel" sequentially across the specimen thickness. These tunnel cracks are assumed for simplicity to be equally spaced edge cracks and to terminate at the interface between the two layers. The normalized crack density $n$ is defined as the ratio of specimen width $w$ to crack spacing $a$, $n = w/a$, see Fig. 2.

### 2.1. Tunneling of large initial flaws

The theory presented in [5] to model crack growth from large flaws is based on energy minimization, and relies on the finite element analysis of the unit cell shown in Fig. 2 to calculate the relevant physical parameters – stress, strain, energy release rate, etc. Fig. 4 succinctly summarizes the salient results of that earlier study. The normalized work of fracture, $W/W_0$, of the multiply cracked composite specimen is shown in Fig. 4(a), as a function of the toughness ratio, $K_{c1}^{\text{eff}}/K_{c2}$. The crack density at failure, $n_{\text{f}}$, as a function of $K_{c1}^{\text{eff}}/K_{c2}$ is shown in Fig. 4(b). $W_0$ represents the work to fracture of a homogeneous reference beam of toughness $K_{c1}$ which fails at initiation of the first crack.

This model suggests that the toughness ratio, $K_{c1}^{\text{eff}}/K_{c2}$, must be larger than a threshold value of about 2 to prevent the first crack in the weak layer from causing specimen failure. Furthermore, for $K_{c1}^{\text{eff}}/K_{c2}$ values in the experimentally observed range 2.5–3.0 [7,8], multiple tunnel cracks lead to an order of magnitude increase in work of fracture above that of a uniform high toughness ($K_{c1}^{\text{eff}}$) beam fractured by propagation of the first crack. We confirmed this theoretical criterion for the development of multiple cracking by

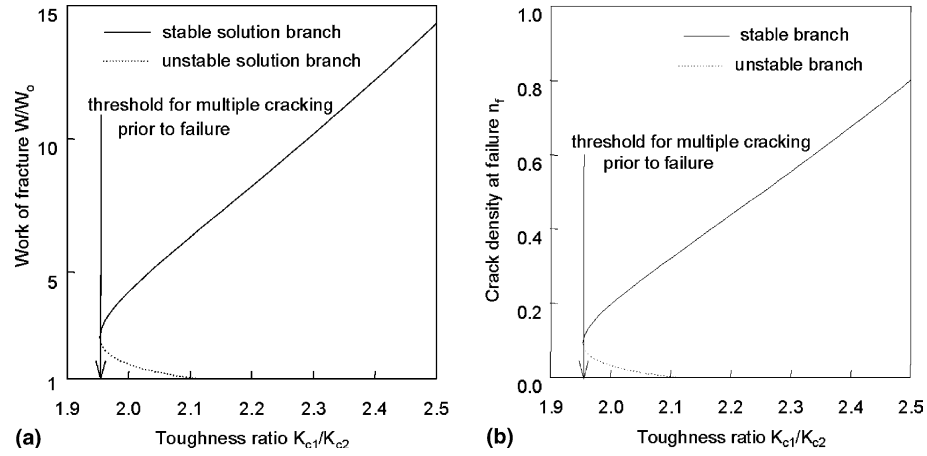


Fig. 4. (a) Normalized work of fracture, $W/W_0$, and (b) crack density at failure, $n_f$ of a composite multiply cracked specimen as a function of the fracture toughness ratio $K_{c1}^{\text{eff}}/K_{c2}$.

performing bend tests on samples that contained residual surface compressive stresses that had been introduced during the grinding stage of preparing specimens from whole shells. [1] (Surface grinding of both ductile and brittle materials invariably gives rise to surface comprehensive stresses.) These specimens fractured without developing multiple tunnel cracks, and were associated with a work of fracture an order of magnitude lower than those that had not been polished. The residual stresses must have produced an increase in the effective toughness of the interface (0.6 MPa $m^{1/2}$, [7,8]) by an amount that renders $K_{c1}^{\text{eff}}/K_{c2}$ less than 2.0 (in other words, the applied stresses must overcome the residual compressive stresses in order for the large inherent flaws to propagate).

In attempting further extensions of this model, it became clear that the toughening effect shown in Fig. 4(a) cannot be extrapolated to very much larger toughness ratios without fatally compromising the model, and could not account for the three-order of magnitude increase in work of fracture. In fact, we discovered that for crack spacings smaller than a certain value, tunnel cracks could not reach the effectively unloaded specimen surface. As shown in Fig. 5, a reproduction of Fig. 3b of [5], at a critical value of tunnel crack density in bend tests of unnotched specimens, short cracks initiate at the interface between the weak and tough middle layers during tensile loading, and grow "backwards" a short distance into the weak layer.

This phenomenon was in fact suggested by the results of the finite element analysis of the configuration shown in Fig. 2, for either applied bending or tensile stress conditions. Fig. 6 shows that for sufficiently small tunnel crack distances (in a specimen subjected to tension), the normalized surface stress between adjacent tunnel cracks becomes compressive! This implies that a crack saturation density must result, and that additional cracks in the weak layer could initiate only at the interface between the weak and tough layer.

[1] In our earlier work [1], the tensile and compressive of the bend bars were as-grown inner and outer shell surfaces.

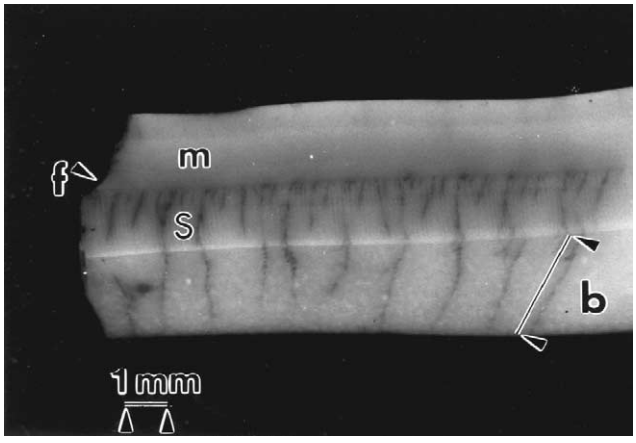


Fig. 5. Micrograph showing dye-penetrated tunnel cracks in the weak layer. The longer cracks are through the thickness and are indicated by symbol *b*; these saturate at a critical density. The short cracks that propagate from the interface between layer m and layer s arrest as a result of the compressive stress that develops between the longer cracks at saturation – see Fig. 6. *f* is the fracture surface.

### 2.2. Tunneling of small initial flaws

The model just described was extended to investigate the possibility of tunneling in the weak layer of a large number of uniformly distributed surface flaws that are very small compared to the layer thickness (Fig. 3(b)). According to linear elastic fracture mechanics, these would extend at a critical stress given by

$$\sigma_{xx} = \sigma_c \equiv Y_2 K_{c2}/\sqrt{c}, \tag{1}$$

where the critical surface stress, $\sigma_c$, depends on the fracture toughness $K_{c2}$ of the weak layer, the length $c$ of the small preexisting flaws, and a geometrical constant, $Y_2$.

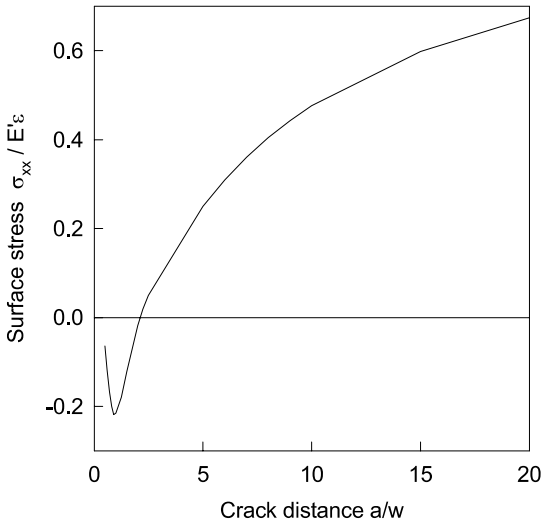


Fig. 6. Surface stress $\sigma_{xx}$ between adjacent cracks in a multiply cracked tensile specimen as a function of the normalized crack distance, $a/w$. $\sigma_{xx}$ is given in units $E'\varepsilon$ of the tensile stress in an uncracked plane strain specimen subjected to the same applied strain $\varepsilon$.

Fig. 7 summarizes the implications of applying the stress-based cracking criterion to the cracking pattern shown in Fig. 2. The critical stress, $\sigma_c$, and the work of fracture, $W$, are normalized with respect to $\sigma_0$ and $W_0$, the failure stress and work of fracture, respectively, of a pre-cracked reference specimen with the higher toughness value, $K_{c1}^{\text{eff}}$. The single precrack represents the catastrophic influence of a large initial flaw in such a specimen. As a result of the surface stress becoming compressive at small crack spacings, Fig. 7(a) shows that the crack density at failure is characterized by a saturation limit even in the most favorable situation of a low strength weak layer; the corresponding work of fracture for this case is shown in Fig. 7(b).

These results clearly illustrate the advantage of large pre-existing defects in the weak layer (discussed in the first part of this section) with respect to work of fracture and flaw tolerance of the composite beam: For a realistic but moderate toughness ratio, say $K_{c1}^{\text{eff}}/K_{c2} \approx 2.5$, and equal thickness layers, the strength ratio $\sigma_0/\sigma_c$ scales proportionally to $(\sqrt{c/t_2}) \cdot (K_{c1}^{\text{eff}}/K_{c2})$. For small surface defects, $c \ll t_2$, and $K_{c1}^{\text{eff}}/K_{c2} \approx 2.5$, this would be less than one – the threshold value for multiple cracking shown in the figure – thus indicating the impossibility of a stress-based multiple cracking mechanism in a composite beam with small surface defects and moderate toughness ratios.

## 3. Large scale bridging in the "tough" layer

Two types of large scale bridging were observed during our experiments. The most important is included in the schematic drawing of Fig. 1(a), which shows an inclined crack path in the tough layer that is favored by the existence of weak interfaces between second-order lamellae. This path is available to one (or more) of the tunnel cracks as it grows across the tough layer. The crack path follows, without significant deviation, the direction dictated by the second-order interfaces, as observed in the tough layer of both notched and unnotched samples. For the latter case, this was already shown in Figure 8a of [1]. However, when a crack propagates along this preferred direction, indicated by the bold arrow in Fig. 1(a), it has to break approximately 50% of the second-order lamellae interfaces – those which are oriented perpendicular to the direction of crack propagation. These perpendicular lamellae behave as reinforcing bars that resist crack opening displacements, and in turn crack propagation. For this reason, fractographs of this region of the specimen,

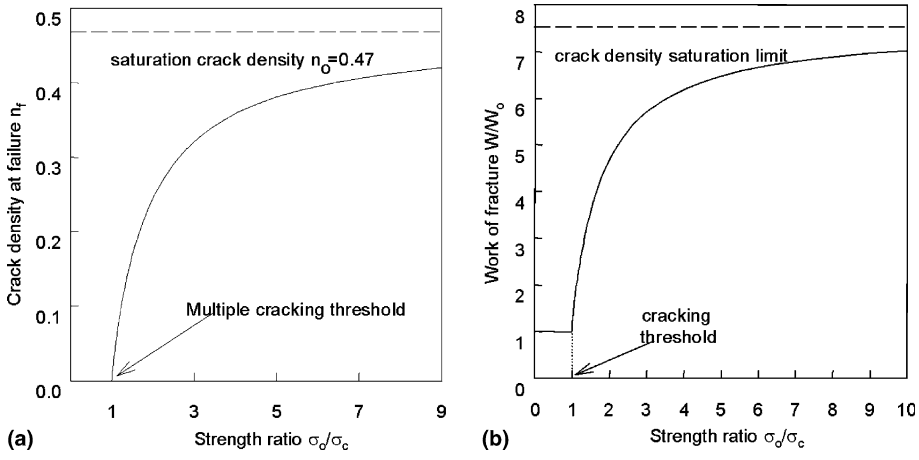


Fig. 7. (a) Crack density at failure as a function of the ratio $\sigma_0/\sigma_c$. $\sigma_c$ represents the critical surface stress in the weak layer for microcracking from small surface flaws. $\sigma_0$ is the failure stress of a uniform reference specimen with the high toughness $K_{c1}$ containing a single precrack of a length equal to half the specimen thickness. (b) Work of fracture for the same situation, given in units of $W_0$, the work of fracture of the pre-cracked reference specimen.

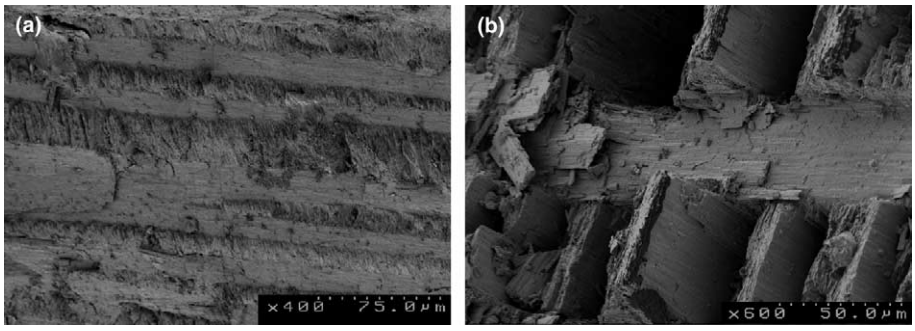


Fig. 8. Fracture surfaces comprised of alternating smooth and rough regions at (a) −120 °C and (b) 200 °C.

Figs. 1(b) and 8, show an alternating pattern of smooth and rough surfaces for specimens tested at −120 °C, Fig. 8(a), room temperature, Fig. 1(b) and 200 °C, Fig. 8(b) (the temperature dependence is discussed below). The smooth features correspond to debonded second-order interfaces parallel to the direction of crack propagation, whereas the rough surfaces correspond to broken second-order lamellae oriented perpendicular to the propagating crack. As discussed next, the amount of pull-out greatly affects the stability of crack propagation within the tough layer, and in turn the work of fracture of the shell.

Before breaking at the end of the bridging zone, the side faces of the bridging "strong" first-order lamellae (comprised of second-order lamellae perpendicular to the direction of crack propagation) slide against the adjacent "weak" first-order lamellae lamellae which are already fractured at their second-order interfaces along the crack (Fig. 9 is a schematic of the pull-out process observed in Fig. 8). This mechanism can be analyzed in terms of established fiber bridging models with frictional

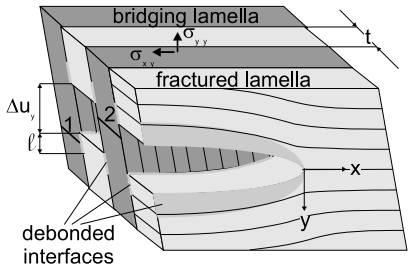


Fig. 9. Bridging zone for frictional sliding along debonded interfaces between fractured (weak) and bridging (strong) first-order lamellae. The front plane is rotated by 45° with respect to Fig. 1a as indicated by the crack-tip coordinate system. The low toughness second-order interfaces in weak lamellae are oriented parallel to the direction of crack propagation but are perpendicular to this direction in adjacent strong lamellae. Debond length, first-order lamellar thickness and mode I crack opening are denoted by $l$, $t$ and $\Delta u_y$, respectively. Depending on strength variations in the bridging lamella, their fracture locus at the end of the bridging zone may be either in the sliding area (1), or between the crack faces of the weak lamella (2). The first case leads to additional energy dissipation by frictional pullout of strong lamella behind the bridging zone. Due to the inclined crack path, the crack is loaded simultaneously in mode I ($\sigma_{yy}$) and mode II ($\sigma_{xy}$).

sliding at fiber–matrix interfaces [10–12]. For equal volume fractions and equal Young's moduli of matrix and fiber, the fiber bridging law derived in these references, which relates the previously defined effective traction on the crack surfaces, $\sigma(\Delta u)$, to the crack opening displacement $\Delta u$, reduces to

$$\sigma(\Delta u) = \left(\frac{E\tau\Delta u}{R}\right)^{1/2}, \tag{2}$$

where $E$, $\tau$ and $R$ denote Young's modulus, a constant fiber frictional stress, and fiber radius, respectively. The toughening contribution is obtained as the area under the $\sigma(\Delta u)$ curve (with $\sigma$ varying from zero to the limiting fiber strength, $\sigma_0$) as

$$J_b = \frac{2R\sigma_0^3}{3E\tau}. \tag{3}$$

As opposed to the situation analyzed in [11], the bridging mechanism in Fig. 9 includes both modes I and II contributions. Nevertheless, Eqs. (2) and (3) can be generalized to the crossed-lamellar structure, as indicated in the Appendix A if $\sigma$ is interpreted as the magnitude of the vector sum of the normal and shear tractions on the crack surfaces, and $\Delta u$ is interpreted as the magnitude of the vector sum of the crack opening and crack sliding displacements. Thus we introduce the following "transformative" terms: matrix → "weak" first-order lamellae, bridging fibers → "strong" first-order lamellae, fiber radius ($R$) → thickness of first-order lamellae, $t$.

For surface roughness-induced "elastic friction" (see Figure 10 [13]), the friction stress between adjacent first-order lamellae should be of order

$$\tau \propto \frac{Eh}{\lambda}, \tag{4}$$

where $h/\lambda$ represents the average normalized surface roughness of the first-order lamellar interfaces (Fig. 10). Thus a toughening contribution

$$J_b = \frac{2t\sigma_0^3}{3E^2h/\lambda}, \tag{5}$$

can be expected. The size of the bridging zone, $L$, can be roughly estimated from the following relation for lim-

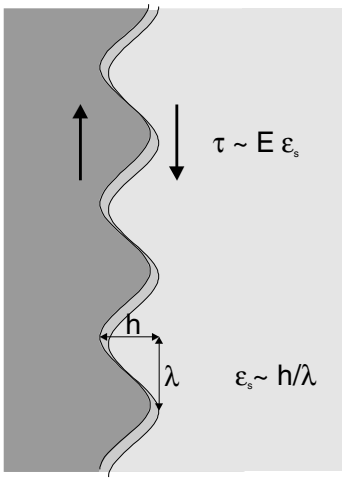


Fig. 10. The surface roughness-induced "elastic friction stress", $\tau$, caused by sliding of adjacent first-order lamellae, is proportional to the product of Young's modulus, $E$, and the average sliding deformation, $\varepsilon_s$. The average sliding deformation, $\varepsilon_s = \Delta u_s/\Delta x$, is calculated from average height, $\Delta u_s = h$, and average spacing, $\Delta x = \lambda$, of surface obstacles.

iting strength, $\sigma_0$, and critical crack opening displacement, $\Delta u_0$, [12]

$$\sigma_0 \propto E\varepsilon \propto E \cdot \frac{\Delta u_0}{L}. \tag{6}$$

Invoking the bridging law, Eq. (2) (with $R = t$), and the friction relation, Eq. (4), we obtain

$$L \propto \frac{t\sigma_0}{\tau} \propto \frac{\sigma_0}{E}\frac{\lambda}{h} \cdot t. \tag{7}$$

Because we do not have reliable experimental information regarding either the friction stress, $\tau$, the normalized surface roughness, $h/\lambda$, or the strength of first-order lamellae, $\sigma_0$, in the necessary orientation, we lump these into an effective parameter $\beta$ and write the cohesive law, which is operative up to a critical crack surface displacement, $\Delta u_0$, and limiting strength $\sigma_0$, as

$$\sigma(\Delta u) = \beta \Delta u^{1/2}. \tag{8}$$

The crack bridging introduces an additional toughening given by

$$J_b = \int_0^{\Delta u_0} \sigma(\Delta u)\, \mathrm{d}(\Delta u) = \frac{2}{3}\beta \Delta u_0^{3/2}. \tag{9}$$

A second type of large scale bridging, which is not modeled in the present paper, was observed in the middle tough layer of the conch shell and is shown in Fig. 11(a). This mechanism involves the development of delamination cracks at the interface between the outer and middle layers that are bridged by intact plates comprised of the middle layer. This phenomenon can be understood and in principle analyzed using the model of Spearing and Evans [10] for misaligned fibers in a fiber–matrix composite (Fig. 11(b), adapted from [10]). For

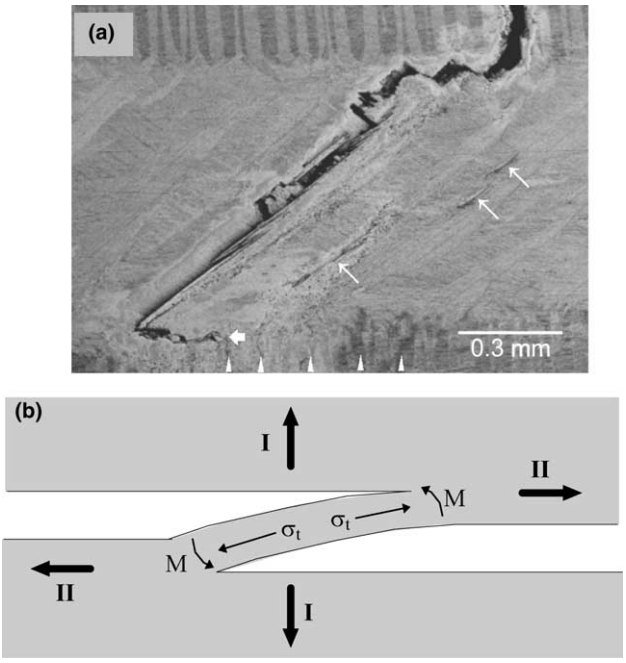


Fig. 11. (a) Ligament bridging a delamination between the middle and outer layers of the shell. The vertical arrows indicate tunnel cracks in the weak outer layer, the inclined arrows microcracks in the strong middle layer; (b) Model for crack bridging by misaligned fibers [11]. According to [11], mode I loading leads to bending (moment M) of the bridging ligament. In general, the crack faces can be loaded by modes I and II tractions, therefore resulting in a tensile load ($\sigma_t$) on the bridging ligament.

mode I loading, such bridging ligaments can be considered as equivalent to small beams loaded by opposite crack faces in bending, and the energy release rate can be obtained from standard beam theory. In contrast to the mode I loaded double cantilever beam specimen analyzed in [10], the deflected crack in the tough layer is subject to mixed mode loading. Thus the bridging lamella deform both in bending (mode-I loading) and in tension (mode-II loading). Therefore, the bridging law given by Spearing and Evans would need to be modified, taking into account combined bending and tensile loading of bridging ligaments. Depending on the mode mixity, the resulting bridging law is expected to be a softening relation (with bridging tractions decreasing as a function of the crack opening displacements) for prevailing mode I loading, or a hardening relation for prevailing mode II loading.

## 4. Finite element analysis of large scale bridging

To quantify the parameters $\beta$ and $\Delta u_0$ for the shell of the conch, and in turn predict the energy dissipation associated with crack bridging, a finite element analysis of a series of experiments was performed using the commercial codes ABAQUS [14] and PATRAN [15] for

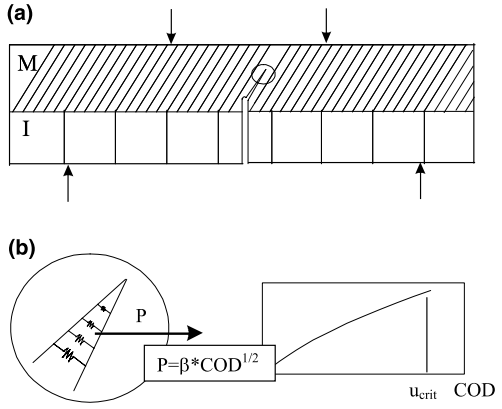


Fig. 12. (a) Schematic of the four-point bend specimen with the notch in the middle layer (M). The inner layer is denoted I. The crack propagates at 45° between second-order interfaces. (b) The bridging tractions across the crack face are simulated by non-linear springs which obey a bridging law of the form $\sigma(\Delta u) = \beta \Delta u^{1/2}$.

pre- and post-processing. The details of the calculation procedure are presented in [7]. A schematic of the two-dimensional plane strain model is shown in Fig. 12. First, trial values are selected for $\beta$ and $\Delta u_0$. As discussed previously, the specimens are isotropic with elastic modulus $E' = 37$ GPa, and are assigned a Poisson ratio equal to 0.3. Crack bridging is achieved by placing non-linear springs that obey the cohesive law, given by Eq. (8), across the surfaces of the crack. As the applied load is increased, the opening of the crack surfaces is monitored and springs are removed if their stretch reaches the critical value $\Delta u_0$. The crack tip is advanced when the total stress intensity factor, which has contributions from the applied loads and the bridging tractions and is determined from the numerically calculated $J$ integral, reaches a value equal to the fracture toughness of the proteinacous interface between first-order lamellae, equal to 0.60 MPa $m^{1/2}$.

Fig. 13 shows that calibration experiment A is well predicted by $\beta = 630$ N $mm^{-5/2}$ and $\Delta u_0 = 5$ μm ($\sigma_0 = 45$ MPa); this figure is reproduced from [8]. These parameters are associated with $J_b = 148$ N/m, a value much larger than the energy release rate involved in the cleavage of the proteinaceous interface embedded in the composite shell, $J_c^{int} = (0.6 \text{ MPa}\sqrt{m})^2/37 \text{ GPa} = 9.7$ N/m. Significantly, these values predict reasonably well the response of specimen B, whose dimensions differ considerably from those of specimen A. These results suggest that crack propagation in the tough middle layer is characterized reasonably well by the crack-bridging model. The energy associated with this process is compared with the finite element calculated energy associated with breaking simulated specimens made of non-biogenic aragonite and of protein in Table 1. Crack bridging requires roughly two orders of magnitude higher energy than the energy required to break a specimen made of non-biogenic aragonite.

The synergistic effects of multiple tunnel cracking in weak layers and fiber bridging in the tough layer is predicted using the finite element method by simulating, with the calibrated cohesive law, the propagation of one of the previously discussed tunnel cracks through the tough middle layer. The load–displacement curve for a typical simulation is shown in Fig. 13, and the energy

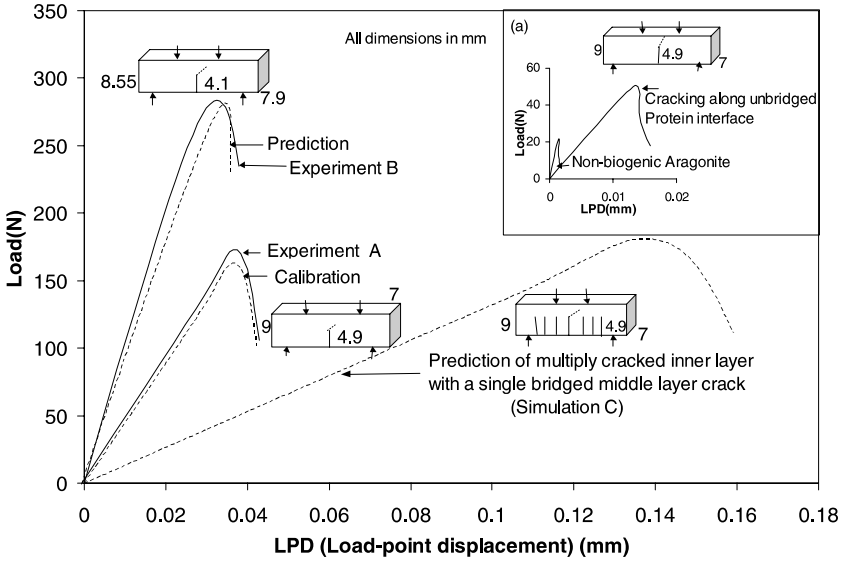


Fig. 13. Experimental and theoretical load–deflection curves for specimens containing middle layer notches from experiments A and B (two different geometries to validate the parameters). The theoretical unnotched beam response (simulation C, involving multiple cracking followed by a single tunnel crack propagating through the bridged middle layer) can be compared with the theoretically predicted response (see inset) of a beam comprised solely of non-biogenic aragonite ($K_C = 0.25$ MPa $m^{1/2}$) or a beam in which cracks propagate unbridged along a mineral–protein interface ($K_C = 0.6$ MPa $m^{1/2}$).

Table 1
Area under the load–displacement curves for the curves in Fig. 13, expressed in units of energy ($10^3$ J)

| Aragonite | Protein interface | Notched specimen | Multiple cracking with bridged crack |
|---|---|---|---|
| 0.07 | 0.4 | 5.8 | 23 |

dissipated is listed in Table 1. This last result shows that the energy required to completely fracture an unnotched shell with a given dimension is roughly 330 times more than the energy required to break a specimen made of non-biogenic aragonite.

This increase is somewhat less than the three-orders increase seen in the experiments in [1]. However we note that the results may depend sensitively on specimen geometry and specimen-to-specimen variation in properties. Furthermore, there may be additional energy dissipation mechanisms that have not been treated in the analysis, e.g. the delamination cracks shown in Fig. 11.

## 5. Ductility of the organic (proteinaceous) interphase

While the volume fraction of the organic phase is modest (a few percent at most), its role in the fracture resistance of the shell cannot be overstated. To quantify the effects of the interphase ductility on the strength and work of fracture of the shell, we performed four points bend tests in a temperature controlled chamber at temperatures ranging from −120 to 200 °C. Unnotched specimens of the type described in [4] were used. We assume that within the range −120 to 200 °C, the mechanical properties of the aragonite do not change, and that there exists a glass transition temperature, $T_g$, for the protein in this temperature range.The load–displacement traces for four representative temperatures are shown in Fig. 14(a)–(d). As expected, the response becomes increasingly "brittle" at low temperatures, as evidenced by the lack of deformation in the post-peak region. The nominal strength goes through a maxima at ~80 °C.

The brittleness can be quantified through the brittleness factor, $F_b$, defined as the area under the load–displacement curve at peak load divided by the total area (this measure has been widely used for other quasibrittle materials such as concrete; it cannot be used to characterize the load–displacement response of ductile materials). As shown in Fig. 15, there appears to be a brittle to ductile transition between 100 and 150 °C, a range consistent with the existence of a glass transition temperature. This explains why the fracture surface of a very brittle specimen tested at −120 °C (Fig. 8(a)) is relatively smooth, indicating a relatively small amount of fiber pullout and crack bridging, as compared to the significant pull-out observed on the fracture surface of a quasi-ductile specimen tested at a higher temperature (Fig. 8(c)). The degree of pull-out at room temperature,

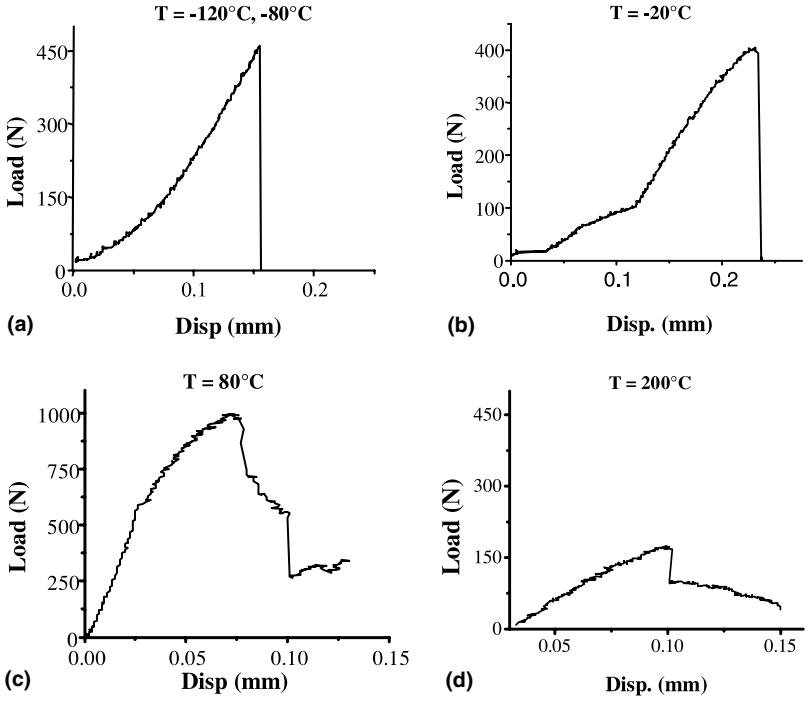


Fig. 14. Load–deflection curve of dry unnotched sample. At low temperatures (A and B), the sample did not show any post peak behavior and the fracture behavior is very "brittle". As the temperature increases, the bridging becomes more efficient. At high temperatures (D), the samples did not show much load-bearing capabilities.

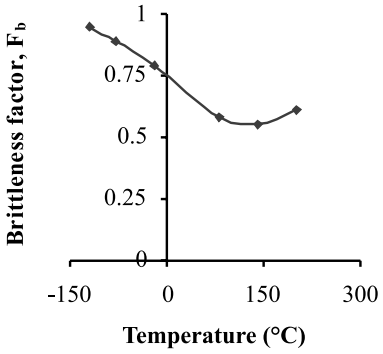


Fig. 15. Brittleness factor as function of temperature.

as shown in Fig. 1(b), is intermediate between that of Fig. 8(b) and (c).

Further insight into the existence of a well-defined $T_g$ for the protein interphase was obtained from dynamic mechanical analysis (DMA), a widely used technique to determine $T_g$ of organic polymers. DMA analysis involves elastic deformation in response to sinusoidally varying vibrational forces of modest amplitude. Part of the energy is stored as potential energy (stored modulus, $G'$) and part is dissipated as heat (loss modulus, $G''$). The loss tangent ($\tan\gamma$), defined as the ratio of the energy dissipated per cycle to the maximum energy stored during cycle, is used to determine $T_g$ of polymers, because it amplifies the difference between the storage and loss moduli.

Using a Rheovibron machine (RMS800, TA Instruments, New Castle, DE) at a frequency of 1 Hz, DMA was undertaken of a $9.5 \times 2.5 \times 42$ mm$^3$ rectangular parallelepiped, with the results shown in Fig. 16. The most prominent peak in the loss tangent is taken as $T_g$ and is approximately 175 °C, in reasonable agreement with the brittle to ductile transition in the brittleness curve.

It is also possible to estimate $T_g$ of proteins from their amino acid contents, using a protocol involving the van der Waals interaction volume of the various amino acids. This has been done for several proteins extracted from wild *S. gigas* shells; $T_g$ is estimated to be ~180 °C from this approach (the details can be found in [4]), in good agreement with $T_g$ determined by DMA.

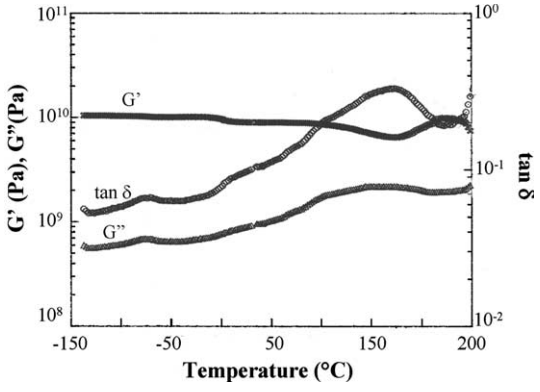


Fig. 16. Storage modulus, loss modulus, and loss tangent as functions of temperature.

## 6. The ACK limit

As discussed by Cox and Marshall [11], the parameters $J_c^{int}$, $J_b$, $\beta$ and $\Delta u_0$ are related to the toughness and notch sensitivity of structures associated with bridged cracks; their magnitudes determine whether failure occurs as a result of catastrophic or non-catastrophic crack propagation.

Cox and Marshall define several parameters that assess the nature of the failure produced by cracks that obey a bridging law of the form of Eq. (8); $\sigma_1$ defines the value of the critical stress for crack extension in the ACK (Aveston–Cooper–Kelly) limit [2], a situation where essentially all crack-bridging ligaments remain intact as a crack propagates across a matrix; $a_m$ defines the non-catastrophic bridging length scale that represents the amount of crack growth necessary to approach the ACK limit; and $a_s$ is the small scale bridging length scale.

For the bridging law of Eq. (8), these parameters become

$$\frac{\sigma_1}{\sigma_0} = \left(\frac{2J_c^{int}}{J_b}\right)^{1/3}, \tag{10}$$

$$a_m = \frac{\pi E'}{4}\left(\frac{3J_c^{int}}{2}\right)^{1/3}\beta^{-4/3}, \tag{11}$$

$$\frac{a_s}{a_m} = \frac{2}{\pi}\left(\frac{\sigma_0}{\sigma_1}\right)^4. \tag{12}$$

As discussed by Cox and Marshall, these provide insight into the type of (bridged) crack propagation that occurs in composite plates of width $w$, be they unnotched, or containing a notch of length, $c_0$. First, non-catastrophic failure gives way to catastrophic failure for $\sigma_1 > \sigma_0$, or rather if $J_c^{int}$ exceeds $J_b$. Second, the fibers' effectiveness increases with increasing $w/a_m$. If the width of a specimen is much less than $a_m$, then bridging effects are negligible, even though the bridging ligaments may be intact all along the crack wake. Third, if $c \gtrsim a_m$, then crack growth from a notch is stable. On the other hand, if the specimen contains a notch that is much less than $a_m$, then crack growth is unstable immediately (or shortly after) the crack emerges from the notch. Finally, if $a_m \ll a_s$, then the ACK limit will be reached in a sufficiently large specimen.

For the conch shell considered here, $w \sim 10$ mm, and the tunnel cracks that are arrested at the interface between the weak and tough layers act as initial notches of length $c_0 \sim 5$ mm. The experimentally calibrated

bridging law parameters yield $\sigma_1/\sigma_0 = 0.5$, $a_s \sim 25$ mm and $a_m \sim 1.3$ mm. Therefore the conch shell is associated with all of the favorable situations described above, as observed experimentally. It is remarkable that besides dissipating energy, the multiple tunnel cracks are also responsible for the subsequent stable propagation of their bridged extensions into the tough middle layer.

## 7. Conclusions

It has been shown through two quantitative micromechanical fracture models that the energy involved in fracturing the shell of the conch *S. gigas* can be partitioned into components, the first associated with multiple cracking of the outer layers of the shell, and the second with crack surface bridging in the middle layer. Moreover, the experimentally calibrated model parameters suggest that the structural configuration of the shell has evolved in a manner that allows inherent cracks to achieve the ACK limit that enables them to propagate in a non-catastrophic manner. Experiments performed at temperatures ranging from −20 to 200 °C demonstrate that the ductility of the proteinaceous interphase of the shell plays a critical role in achieving this desired limit.

## Acknowledgements

This research was supported by EPRI under Contract UBP900424. H.K. was supported by a 1996/97 Schloessmann-Fellowship of the Max-Planck-Society (Germany); he further appreciates useful discussions with Dr. Brian Cox and Dr. Michael C. Shaw during a visit at Rockwell International Science Center, Thousand Oaks (CA). We thank Dr. Xiao-Wei Su for providing Fig. 1(b), (c) and (d) and Fig. 11(a).

## Appendix A. Small scale bridging law for the crossed-lamellar structure

In this section we derive a micromechanics-based formula that approximates the forces provided by the first and second-order lamellae in resisting the crack opening displacements of a crack as it propagates in the strong layer. It is shown that while these crack-bridging features have plate-like geometries, the functional form of the bridging law is similar to ones derived for brittle-matrix composites involving circular fibers [11,16]. To this end, we first invoke global equilibrium of the fractured (weak) first-order lamellae (Fig. 17) to obtain

$$\sigma_{yi} \cdot t = 2\tau_{zi} \cdot l \quad (i = x, y). \tag{A.1}$$

Here, $l$ denotes the sliding distance, $t$ the thickness of the first-order lamellae and $\sigma_{yi}$ the applied stress at the boundary to the non-sliding region. The traction components $\sigma_{yy}$ and $\sigma_{yx}$ lead to mode I and mode II crack-tip behavior, respectively. The corresponding frictional stress components $\tau_{yz}$ (for mode I) and $\tau_{xz}$ (for mode II) are considered to be material constants which characterize the interface. Eq. (A.1) is based on the assumption that fractured and bridging lamellae at the boundary of the sliding zone are loaded by uniform tractions, $\sigma_{yi}^{(f)}(l) = \sigma_{yi}^{(b)}(l) = \sigma_{yi}$.

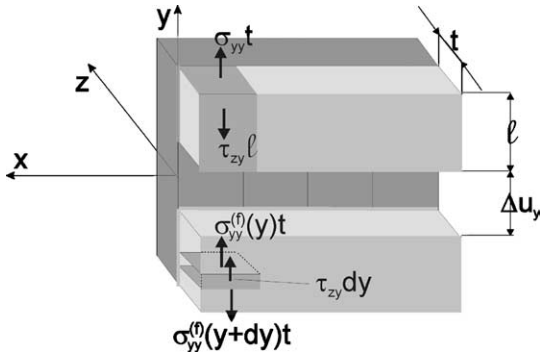


Fig. 17. Friction force equilibrium in the $y$-direction during mutual sliding of debonded first-order lamellae in the sliding region of the bridging zone. The equilibrium in the $x$-direction can be considered in the same way.

Assuming symmetry, the crack opening displacement can be defined as twice the displacement of the fractured lamellae at the crack surface, $u_i^{(f)}(0)(i = x, y)$. The displacement of the bridging lamella, $u_i^{(b)}(y)$, is obviously zero at the crack surface ($y = 0$) and equal to $u_i^{(f)}(l)$ at the end of the sliding zone ($y = l$). Therefore, the crack opening displacement ($\Delta u_y$ for mode I and $\Delta u_x$ for mode II) can be calculated from

$$\frac{\Delta u_i}{2} = [u_i^{(f)}(0) - u_i^{(f)}(l)] - [u_i^{(b)}(0) - u_i^{(b)}(l)] = \int_0^l \frac{\Delta\sigma_{yi}^{(bf)}(y)}{\tilde{E}}\,\mathrm{d}y \quad (i = x, y), \tag{A.2}$$

where the stress difference between bridging and fractured lamellae is denoted by $\Delta\sigma_{yi}^{(bf)}$, and $\tilde{E}$ is equal to Youngs modulus, $\tilde{E} = E$, for $i = y$ and equal to the shear modulus, $\tilde{E} = G$, for $i = x$.

Local equilibrium of a small part of the fractured or bridging lamella over a small distance of the sliding region requires (Fig. 17)

$$t \cdot \mathrm{d}\sigma_{yi}^{(f)}(y) = 2\tau_{zi} \cdot \mathrm{d}y \quad \text{and}$$
$$t \cdot \mathrm{d}\sigma_{yi}^{(b)}(y) = -2\tau_{zi} \cdot \mathrm{d}y \quad (i = x, y), \tag{A.3}$$

and therefore

$$t \cdot \frac{\mathrm{d}\Delta\sigma_{yi}^{(bf)}(y)}{\mathrm{d}y} = -4\tau_{zi} \quad (i = x, y). \tag{A.4}$$

After partial integration of Eq. (A.2), we obtain the crack opening displacement as

$$\Delta u_i = \frac{4\tau_{zi} l^2}{\tilde{E} t} \quad (i = x, y). \tag{A.5}$$

Eq. (A.3) can be used to eliminate the sliding distance ($l$). The bridging law follows as

$$\sigma_{yi}(\Delta u_i) = \left( \frac{\tilde{E}\tau_{zi} \cdot \Delta u_i}{t} \right)^{1/2} \quad (i = x, y). \tag{A.6}$$

Explicitly for modes I and II, this equation is written as

$$\sigma_{yy}(\Delta u_y) = \left( \frac{E\tau_{yz} \cdot \Delta u_y}{t} \right)^{1/2} \quad \text{for mode I,} \tag{A.7}$$

and

$$\sigma_{yx}(\Delta u_x) = \left( \frac{G\tau_{zx} \cdot \Delta u_x}{t} \right)^{1/2} \quad \text{for mode II.} \tag{A.8}$$

The particular values of the friction constants, $\tau_{zy}$ and $\tau_{zx}$, as well as the values of the moduli, $E$ and $G$, are unknown. In order to simplify the simulations, we have postulated a bridging law which combines (A.7) and (A.8) in a single equation

$$\sigma(\Delta u) = \left( \frac{E\tau \cdot \Delta u}{t} \right)^{1/2}, \tag{A.9}$$

where

$$\Delta u = \sqrt{\Delta u_x^2 + \Delta u_y^2} \quad \text{and} \quad \sigma = \sqrt{\sigma_{xy}^2 + \sigma_{yy}^2}, \tag{A.10}$$

are the magnitude of the crack opening displacement vector and the total bridging traction, respectively, and $E\tau$ represents the product of an efficient modulus with an efficient friction stress.

## References


[1] Kuhn-Spearing LT, Kessler H, Chateau E, Ballarini R, Heuer AH, Spearing SM. J Mater Sci 1996:6583.
[2] Aveston J, Cooper GA, Kell A. Properties of fiber composites. In: Conf Proc, 15, National Physical Laboratory. IPC Science and Technology Press; 1971.
[3] Su XW, Zhang DM, Heuer AH. Chemistry of Materials 2004;16:581.
[4] Naisorrou M. Characterization of the damage mechanisms and environmental effects on the mechanical properties of the shell of Strombus gigas. MS thesis, Department of Materials Science and Engineering, Case Western Reserve University, August 2001.
[5] Kessler H, Ballarini R, Mullen RL, Kuhn LT, Heuer AH. Comp Mater Sci 1996;5:157.
[6] Kessler H, Ballarini R, Mullen RL, Kuhn LT, Heuer AH. Comp Mater Sci 1996;6:353.
[7] Kamat S. Toughening mechanisms in laminated composites: a biomimetic study in mollusk shells. PhD thesis, Department of Materials Science and Engineering, Case Western Reserve University, August 2000.
[8] Kamat S, Su X, Ballarini R, Heuer AH. Nature 2000;405:1036.
[9] Hutchinson JW, Suo Z. Advances in applied mechanics, vol. 29, 1990. p. 63.
[10] Spearing SM, Evans AG. Acta Metall Mater 1992;40:2191.
[11] Cox BN, Marshall DB. Acta Metall Mater 1994;42:341.
[12] Bao G, Suo Z. Appl Mech Rev 1992;24:355.
[13] Raj R, Ashby MF. Met Trans 1971;2:1113.
[14] ABAQUS, Hibbitt, Karlsson & Sorensen, Inc., Pawtucket, RI.
[15] MSC PATRAN, MacNeal Schwindler Corporation, Los Angeles, CA.
[16] Hutchinson JW, Jensen HM. Mech Mater 1990;9:139.